JAEA-Data/Code
2015-033
DOI:10.11484/jaea-data-code-2015-033

Measurement of High-energy Neutron Fluxes and Spectra around the J-PARC Mercury Spallation Neutron Target using Multi-foil Activation Method

Yoshimi KASUGAI, Masahide HARADA, Tetsuya KAI, Motoki OOI
Shin-ichiro MEIGO and Fujio MAEKAWA

Materials and Life Science Division
J-PARC Center
Sector of Nuclear Science Research

March 2016

Japan Atomic Energy Agency

日本原子力研究開発機構

JAEA-Data/Code

本レポートは国立研究開発法人日本原子力研究開発機構が不定期に発行する成果報告書です。
本レポートの入手並びに著作権利用に関するお問い合わせは、下記あてにお問い合わせ下さい。
なお、本レポートの全文は日本原子力研究開発機構ホームページ（http://www.jaea.go.jp）
より発信されています。

国立研究開発法人日本原子力研究開発機構 研究連携成果展開部 研究成果管理課
〒319-1195 茨城県那珂郡東海村大字白方 2 番地4
電話 029-282-6387, Fax 029-282-5920, E-mail:ird-support@jaea.go.jp

This report is issued irregularly by Japan Atomic Energy Agency.
Inquiries about availability and/or copyright of this report should be addressed to
Institutional Repository Section,
Intellectual Resources Management and R&D Collaboration Department,
Japan Atomic Energy Agency.
2-4 Shirakata, Tokai-mura, Naka-gun, Ibaraki-ken 319-1195 Japan
Tel +81-29-282-6387, Fax +81-29-282-5920, E-mail:ird-support@jaea.go.jp

JAEA-Data/Code 2015-033

Measurement of High-energy Neutron Fluxes and Spectra around the J-PARC Mercury Spallation Neutron Target using Multi-foil Activation Method

Yoshimi KASUGAI[+1], Masahide HARADA, Tetsuya KAI, Motoki OOI, Shin-ichiro MEIGO and Fujio MAEKAWA[+2]

Materials and Life Science Division
J-PARC Center
Sector of Nuclear Science Research
Japan Atomic Energy Agency
Tokai-mura, Naka-gun, Ibaraki-ken

(Received December 28, 2015)

The high-energy neutron fluxes and spectra around the mercury spallation neutron source at the Materials and Life Science Experimental Facility (MLF) of J-PARC were measured by the multi-foil activation method. The threshold energies of neutron reactions utilized in this experiment covered from 0.1 to 50 MeV. The foil irradiation was carried out on the first beam-run of MLF from May 30th to 31th, 2008. After the irradiation, the induced radioactivity of each foil was measured using an HPGe detector, and the neutron-induced reaction-rate distribution around the mercury target was determined. Using these data, the high-energy neutron fluxes and spectra were deduced with unfolding method in which the neutron spectra calculated with PHITS code were used as the initial-guess spectra. By comparison between the initial and the unfolded spectra, it was shown that most of the calculation results, which had been the basis of the neutronics design of the MLF target assembly, were consistent with the experimental data within ±30%.

Keywords: J-PARC, MLF, JSNS, Neutron Source, Mercury, Spallation Reactions, Threshold Reaction Rate, High-energy Neutron Spectra, Multi-foil Activation Method, PHITS, Unfolding

---

[+1] Safety Division, J-PARC Center

[+2] Nuclear Transmutation Division, J-PARC Center

JAEA-Data/Code 2015-033

J-PARC 水銀核破砕中性子源まわりにおける多数箔放射化法を用いた高エネルギー中性子束とスペクトルの測定

日本原子力研究開発機構　原子力科学研究部門
J-PARC センター　物質・生命科学ディビジョン

春日井　好己[+1]・原田　正英・甲斐　哲也・大井　元貴・明午　伸一郎・前川　藤夫[+2]

（2015 年 12 月 28 日受理）

J-PARC、物質・生命科学実験施設（MLF）の水銀を使った核破砕中性子源周りの高エネルギー中性子束及びスペクトルを、多数箔放射化法で測定した。この実験で使った中性子反応のしきい値は 0.1 から 50 MeV であった。実験における箔の照射は、2008 年 5 月 30 日から 31 日にかけて実施された MLF における初めてのビーム運転の際に行われたものである。照射後、各金属箔の放射能を HPGe 検出器で測定し、中性子誘導反応のターゲット周りにおける反応率分布のデータを得た。これらのデータを使い、各測定位置における高エネルギー中性子束及びスペクトルをアンフォールディング法で導出した。その際、初期スペクトルとして PHITS による計算値を用いた。初期スペクトルとアンフォールディングスペクトルを比較したところ、計算結果（これは MLF のターゲット集合体の中性子工学設計の基礎となったものであるが）は、実験値に±30%で一致することがわかった。

J-PARC センター：〒319-1195 茨城県那珂郡東海村大字白方２－４
[+1] J-PARC センター 安全ディビジョン
[+2] J-PARC センター 核変換ディビジョン

Contents

1. Introduction 1
2. Experiment 2
2.1 Activation Foil Setup 2
2.2 Irradiation 2
2.3 Activity Measurement 2
2.4 Deduction of the Reaction Rates 3
2.5 Error Estimation 4
3. Results 5
3.1 Reaction Rate Distribution 5
3.2 Deduction of Neutron Spectra 5
4. Summary 6
Acknowledgements 7
References 8
Appendix A Measurement of ^{24}Na Induced in Aluminum Foils using an Imaging Plate 26
Appendix B Deduction of the Irradiation Factor F_{irr} when the Proton Beam Intensity is Constant in Time 27

目次

1. はじめに 1
2. 実験 2
2.1 放射化箔の配置 2
2.2 照射 2
2.3 放射能測定 2
2.4 反応率の導出 3
2.5 誤差の算出 4
3. 結果 5
3.1 放射化率の分布 5
3.2 中性子スペクトルの導出 5
4. まとめ 6
謝辞 7
参考文献 8
付録 A アルミニウム箔に生成した ^{24}Na のイメージングプレートを使った定量 ... 26
付録 B 陽子ビーム強度が時間的に一定の場合の照射因子 F_{irr} の導出 27

1. Introduction

Materials and Life Science Experimental Facility (MLF) in J-PARC[1)] is a multipurpose experimental facility equipped with two kinds of secondary-particle sources: a muon source and a neutron source. The secondary neutrons are produced by bombarding a mercury target with the pulsed proton beam accelerated to 3 GeV by the linac and the rapid cycling synchrotron (RCS). The final goal of the incident proton beam intensity is 1 MW. The high-energy neutrons generated from the mercury target are moderated in the ultra-low-temperature-hydrogen moderators and are supplied to neutron beam lines to be used for various kinds of material analysis.

The first-beam run of MLF was carried out on May 30 and 31 in 2008. At this chance, the realistic evaluation of the neutronics performance was important mission for the purpose of validation of the neutron source design based on Monte Carlo simulation. Therefore, on the first beam run, we conducted on the following measurements:

(1) High-energy neutron spectra around the mercury target vessel,

(2) Cold neutron flux and spectra at a neutron beam line.

The former one, which is called "source neutron spectra", is important as the start point of neutron transportation because the source-neutron properties make a great impacts on the final goal of the transportation such as the cold-neutron character at the neutron beam line and the shielding performance of the neutron target station as a steel-and-concrete complex. The measurement was carried out with multi-foil activation method. The multi-foil stacks were pasted at the various positions on the surface of the mercury target vessel before the first beam operation. The proton beam operation dedicated to this experiment was done on May 31. After the beam operation, the foils were removed from the vessel, and the induced activities were measured using an HPGe detector.

The measurement on item (2) was carried out using the beam line No.10, called NOBORU[2)], as the first neutron detection of MLF on May 30, and a neutron beam pulse was successfully detected.[3)]

In this report, we focus on the measurement of the source neutron spectra and report the procedure, results and analysis. In the former part of Chapter 2, the experimental procedure on the activation-foil setup, neutron irradiation, and activity measurement are shown. In the latter part, the process of the activation data is shown. In Chapter 3, the reaction-rate data obtained by processing the activation data are shown, and the high-energy neutron spectra are deduced using unfolding method[4)]. The comparisons between experimental data and the calculation results are also mentioned in this chapter. Finally the summary of this report is given in Chapter 4.

2. Experiment

2.1 Activation Foil Setup

The mercury target vessel consists of the mercury vessel and the safety hull with cooling -water channel; the mercury vessel is covered by the safety hull as shown in Fig. 1.

Before the first beam run, stacks of indium, aluminum, niobium and bismuth foils were pasted at various positions on the surface of the safety hull. The thulium foils were also installed to the stacks pasted at the former positions. The size and weight of each kind of foil are tabulated in Table 1, and the positions of the sample stacks are shown in Fig. 2. The stacks were pasted on every side, "Up", "Down", "East" and "West", at the distance 75, 160, 255, 370, 455 and 750 mm from the incident-beam surface. An aluminum foil was pasted on the beam-incident surface in order to measure the incident-beam profile by the activation. The photographs of the sample set-up are presented in Fig. 3.

2.2 Irradiation

The foil irradiation was carried out through the first-beam run on May 30th and 31th, 2008. The history of the beam intensity is shown in Fig. 4. On May 30th, the first-beam event and the conditioning operation were performed with one-pulse operation. On May 31th, the beam operation dedicated for the foil irradiation was implemented. On the dedicated run, 2000 pulses corresponding to 8.4×10^{14} protons were bombarded with the neutron target. Consequently the total number of the incident protons through the whole beam run was 1.0×10^{15} protons.[i]

2.3 Activity Measurement

The activities of the radioactive products were measured using an HPGe detector. The full-energy-peak efficiency was calibrated at the distance of 5 cm from the detector surface; we called it "the standard position". In order to measure a lot of foils efficiently and get good statistics of counting, the irradiated foils were positioned at distance of 0.5 cm from the detector surface; we called it "the close positions". In general, it is difficult to determine the gamma-ray detection efficiencies precisely at positions close to detector surface because it is too sensitive for setting position of samples and the sum effect of cascade-coincidence. Therefore, we determined the

[i] The total number of the incident protons was adjusted in order to keep accessibility of persons around the target vessel after the beam operation because we had to remove the foils by hand after the beam operation.

detection efficiencies at the close position by measuring the counting ratios between the close positions and the standard position using the samples whose activities were relatively higher.[ii]

An imaging plate (IP) was also used for measurement of ^{24}Na induced in the aluminum foils. The detail of the measurement is shown in Appendix A.

2.4 Deduction of the Reaction Rates

We determined the reaction rates in Table 2 from the activation data. The excitation functions of the reactions[5] are shown in Fig. 5. The reaction rates *RR* were deduced using the following equation:

$$RR = \frac{C\lambda}{NF_{irr}e^{-\lambda t_c}(1-e^{-\lambda t_m})I\epsilon} \quad , \tag{1}$$

where

- C: Gamma-ray peak counts,
- λ: Decay constant of a product [s^{-1}],
- N: Number of target nucleus,
- t_c: Cooling time [s],
- t_m: Measurement time [s],
- I: Gamma-ray branching ratio,
- ε: Full-energy-peak efficiency of a gamma-ray.

The decay constants and the gamma-ray branching ratios[6] used in this work are shown in Table 2. In the equation (1) , F_{irr} is an irradiation factor defined as follows:

$$F_{irr} = \sum_{n=0}^{N-1} I_p(t_n)\left(1-e^{-\lambda\Delta t}\right)e^{-\lambda\{t_f-(t_n+\Delta t)\}} \quad , \tag{2}$$

where

- Δt: Sampling time,
- t_i: Irradiation start time,
- t_f: Irradiation termination time,
- t_n: $= n\Delta t$
- $I_p(t_n)$: Number of incident protons per second averaged between t_n and $t_n+\Delta t$.

In this equation, $N = (t_f - t_i)/\Delta t$, and we set Δt= 300 s. The factor $I_p(t_n)(1-e^{-\lambda\Delta t})$ corresponds to the generation of products between t_n and $t_n+\Delta t$, and $e^{-\lambda\{t_f-(t_j+\Delta t)\}}$ corresponds to

[ii] The close-to-standard efficiency ratios are largely depends on the following factors: (i) shapes, size and thickness of samples, (ii) property of gamma-ray cascade decay. Therefore the measurement needs to be done once at least for each kind of sample.

the decay of the elements from $t_n+\Delta t$ to the irradiation termination t_f. Supposing that $I_p(t_n) = I_p$ is constant, the factor F_{irr} reduced to $I_p(1 - e^{-\lambda(t_f - t_i)})$.[iii]

2.5 Error Estimation

Systematic and statistical errors were considered for deduction of the reaction-rate data. The systematic errors included errors of the detection-efficiency calibrations (±5-9%) and the nuclear data of gamma-ray branching ratios (5% at a maximum). The statistical errors were 25% at a maximum while the most of them are less than 5%. The total relative-errors were deduced as

$$\delta_t^2 = \sum_i \delta_i^2 \quad . \tag{3}$$

The value of δ_i is the relative error for i'th item.

The data deduced from the activation measurements of the irradiated foils are shown in Table 3 for all reactions and positions with the total errors.

Note that the total errors shown in Table 3 do not include the error coming from the number of incident protons because that does not contributes to the comparison among the reaction-rate data. The number of incident protons was measured using the current transformer located at the closest position from the proton beam window, and the relative error δ_p was assumed to ±10%. If you use them as absolute reaction-rate values, you should consider that the total errors (δ_t') become to the following[iv] :

$$\delta_t' = \sqrt{\delta_t^2 + \delta_p^2} \quad . \tag{4}$$

[iii] Deduction of the equation is shown in the Appendix B.

[iv] The values of δ_t can be calculated as (Error)÷(Reaction Rate) in Table 3.

3. Results

3.1 Reaction Rate Distribution

The reaction-rate distributions for ^{209}Bi(n, 4n)^{206}Bi are shown in Fig. 6. The proton-beam profile was obtained using the activation of the aluminum foil pasted at the beam incident surface. The radioactivity distribution of the aluminum foil was transferred to an IP after the irradiation. The IP image of the aluminum foil is shown in Fig. 7. The effective center of the profile slightly shifted to "down" and "east", so the reaction rates at the "down" positions were larger than those of the "up" positions. Similarly the reaction rates at the "East" positions were larger than those of the "West" positions.

3.2 Deduction of Neutron Spectra

The high-energy neutron spectrum at each position was deduced using the unfolding method with the SAND-II code[4]. The initial guess spectra were calculated using PHITS code[7] with 3-dimentional geometry model including the target vessel and other components around the target such as moderators, reflectors and shielding. The calculation model and the calculation parameters were mentioned in Ref. 8) in detail. The same proton beam condition shown in Fig.7 was considered. The neutron spectra for the initial guess were calculated by track length tallies. The statistical errors at each energy bin (5% of 1 decade in logarithm scale) were within 5 % below 100 MeV and around 20% above 100 MeV. In Fig. 8, the initial guess and adjusted spectra are shown with the C/E-values, the ratios between the calculated and experimental reaction-rate, where the calculated reaction-rate are the integration of the product of the neutron spectrum and the cross section at individual energy bin over whole energy range.[v] It is shown that most of the C/E-values are ranged from 0.7 to 1.3, indicating that the initial-guess spectra calculated with the PHITS code are quite consistent with the experimental data within ±30%.

[v] Actually, the reaction rates were calculated using following: $RR = \sum \phi(E)\sigma(E)\Delta E$, where RR=(Reaction Rate), E=(Neutron Energy), ΔE=(Neutron-Energy Bin), $\phi(E)$=(Neutron Flux from E to $E+\Delta E$), and $\sigma(E)$=(Cross Section).

4. Summary

The high-energy neutron fluxes and spectra around the mercury target of the pulsed spallation neutron source of J-PARC were measured by the multi-foil activation method, where the threshold energies of neutron reactions ranged from 0.1 to 50 MeV. The foil irradiation was carried out for the first beam-run of MLF from May 30 to 31, 2008. After the irradiation, the induced radioactivity of each foil was measured using an HPGe detector to determine the neutron-induced reaction-rate distribution around the mercury target. Moreover, the high-energy neutron fluxes and spectra were deduced with the unfolding method using the SAND-II code, in which the initial guess spectra were calculated with the PHITS code. As a result of the comparison between the initial and the unfolded spectra, it was concluded that the calculated results were in good agreement with the experimental one within ±30%.

Acknowledgements

The authors would like to thank the J-PARC accelerator operation team and the stuff of the Neutron Source Section for the successful first-beam operation. We are grateful to Drs. Masatoshi Futakawa and Masanori Kaminaga, who were the leader and the deputy leader of the Neutron Source Section at the first-beam operation, for their powerful support to this work. Dr. Hiroshi Takada, who is the current leader of the Neutron Source Section, gave us useful advice for this report. We are also thankful to Dr. Yujiro Ikeda, who was a head of the Materials and Life Science Division at that time, for his important suggestion to this experiment. Finally, we would like to give sincere thanks to Prof. Noboru Watanabe, who passed away in 2015, for leading us to creation of the world's top pulsed neutron source.

References

1) J-PARC (Japan Proton Accelerator Complex), https://j-parc.jp/index-e.html

2) Oikawa, K., Maekawa, F., Harada, M., Kai, T., Meigo S., Kasugai, Y., Ooi, M., Sakai, K., Teshigawara, M., Hasegawa, S., Futakawa M., Ikeda, Y. and Watanabe, N., Design and application of NOBORU - NeutrOn Beam line for Observation and Research Use at J-PARC, Nucl. Instrum. Methods Phys. Res. A589, 2008, pp. 310-317.

3) Maekawa, F., Harada, M., Oikawa, K., Teshigawara, M., Kai, T., Meigo, S., Ooi., M., Sakamoto, S., Takada., H., Futakawa., M., Kato., T., Ikeda., Y., Watanabe., N., Kamiyama., T., Torii., S., Kajimoto, R. and Nakamura., M., First neutron production utilizing J-PARC pulsed spallation neutron source JSNS and neutronics performance demonstrated, Nucl. Instrum. Methods Phys. Res. A620, 2010, pp. 159-165.

4) McElroy, W. N., Berg S., and Gigas G., Neutron-flux spectral determination by foil activation, Nucl. Sci. Eng., 27, 1967, pp. 533-541.

5) Maekawa, F., Möllendorff, U., Wilson, H., Wada, M., and Ikeda, Y., Production of a dosimetry cross section up to 50 MeV, Reactor Dosimetry; Radiation Metrology and Assessment, ASTM, STP1398, 2001, pp. 417-424.

6) Firestone R. B., Shirley, V. S. (Eds.), Table of Isotopes, 8th Edition, 1999 Updated, John Wiley & Sons. Inc., N.Y., (1996).

7) Sato, T., Niita, K., Matsuda, N., Hashimoto, S., Iwamoto, Y., Noda, S., Ogawa, T., Iwase, H., Nakashima, H., Fukahori, T., Okumura, K., Kai, T., Chiba, S., Furuta, T. and Sihver, L., Particle and Heavy Ion Transport Code System PHITS, Version 2.52, J. Nucl. Sci. Technol. Vol. 50, No. 9, 2013, pp. 913-923.

8) Harada, M., Maekawa, F., Oikawa, K., Meigo, S., Takada, H., and Futakawa, M., Application and Validation of Particle Transport Code PHITS in Design of J-PARC 1 MW Spallation Neutron Source, Prog. Nucl. Sci. Technol., Vol. 2, 2011, pp. 872-878.

Table 1 Nominal weight, shape, size and thickness of foils

Material	Weight	Shape	Size	Thickness
In	1.6 g	Square	1.5 cm, 1.5 cm	1 mm
	3.0 g	Square	2 cm, 2 cm	1 mm
Al	0.21 g	Disk	1 cm in diameter	1 mm
Nb	0.66 g	Disk	1 cm in diameter	1 mm
Bi	2.5 g	Disk	1.5 cm in diameter	1.5 mm
Tm	0.9 g	Square	1 cm, 1 cm	1 mm

Table 2 Reactions with high-energy neutrons and the decay data of the products

	Reaction		Q-value [MeV]	E_{th} [MeV][a)]	Half-life	Energy [keV]	Intensity
^{115}In	(n, n')	^{115m}In	-0.34	0.34	4.486 h	336.2[b)]	45.9%
^{27}Al	(n, α)	^{24}Na	-3.13	3.25	14.959 h	1368.6	100%
^{93}Nb	(n, 2n)	^{92m}Nb	-8.97	9.06	10.15 d	934.5	99.07%
^{209}Bi	(n, 4n)	^{206}Bi	-22.45	22.56	6.243 d	803.1	98.9%
	(n, 5n)	^{205}Bi	-29.48	29.63	15.31 d	703.4	31.1%
	(n, 6n)	^{204}Bi	-37.90	38.08	11.22 h	374	81.8%
	(n, 7n)	^{203}Bi	-45.12	45.34	11.76 h	820.3	29.6%
^{169}Tm	(n, 2n)	^{168}Tm	-8.03	8.08	93.1 d	816.0	48.99%
	(n, 3n)	^{167}Tm	-14.87	14.96	9.25 d	207.8	41%
	(n, 4n)	^{166}Tm	-23.60	23.74	7.20 h	778.8	18.9%
	(n, 5n)	^{165}Tm	-30.63	30.82	1.253 d	242.9	35.5%

a) E_{th}: Threshold energy.
b) The contribution of ^{115m}Cd ($T_{1/2}$ = 44.6 d) produced via ^{115}In(n, p)^{115m}Cd reaction to 336 keV gamma-ray counts were taken into consideration in the analysis.

Table 3(a) Reaction rates on the "Up" side of the target vessel

Position Surface	Dist.	Reaction Rates [Nucleus^{-1}Proton^{-1}] ^{115}In(n, n')^{115m}In	^{27}Al(n, α)^{24}Na	^{93}Nb(n, 2n)^{92m}Nb
Up	75	8.9(7)×10^{-27}	4.81(25)×10^{-28}	1.30(7)×10^{-27}
Up-East	160	3.4(4)×10^{-27}	1.31(7)×10^{-28}	4.2(21)×10^{-28}
Up-West	160	3.4(4)×10^{-27}	1.41(8)×10^{-27}	3.5(18)×10^{-28}
Up	255	6.2(5)×10^{-27}	2.80(15)×10^{-28}	7.7(4)×10^{-28}
Up	370	3.4(4)×10^{-27}	1.56(9)×10^{-28}	4.22(22)×10^{-28}
Up	455	2.22(24)×10^{-27}	9.7(5)×10^{-29}	2.63(14)×10^{-28}
Up	750	3.3(4) ×10^{-28}	1.57(9)×10^{-29}	4.52(24)×10^{-29}

Position Surface	Dist.	Reaction Rates [Nucleus^{-1}Proton^{-1}] ^{209}Bi(n, 4n)^{206}Bi	^{209}Bi(n, 5n)^{205}Bi	^{209}Bi(n, 6n)^{204}Bi	^{209}Bi(n, 7n)^{203}Bi
Up	75	1.48(7)×10^{-27}	1.13(7)×10^{-27}	7.0(5)×10^{-28}	3.51(27)×10^{-28}
Up-East	160	7.1(4)×10^{-28}	5.1(3)×10^{-28}	3.60(28)×10^{-28}	1.83(19)×10^{-28}
Up-West	160	5.43(27)×10^{-28}	3.86(24)×10^{-28}	2.77(22)×10^{-28}	1.41(14)×10^{-28}
Up	255	1.13(6)×10^{-27}	8.9(5)×10^{-28}	5.9(4)×10^{-28}	3.20(25)×10^{-28}
Up	370	6.7(3)×10^{-28}	5.2(3)×10^{-28}	3.75(29)×10^{-28}	2.10(22)×10^{-28}
Up	455	4.28(22)×10^{-28}	3.43(22)×10^{-28}	2.27(18)×10^{-28}	1.53(15)×10^{-28}
Up	750	7.6(4)×10^{-29}	6.2(4)×10^{-29}	4.1(4)×10^{-29}	2.1(3)×10^{-29}

Position Surface	Dist.	Reaction Rates [Nucleus^{-1}Proton^{-1}] ^{169}Tm(n, 2n)^{168}Tm	^{169}Tm(n, 3n)^{167}Tm	^{169}Tm(n, 4n)^{166}Tm	^{169}Tm(n, 5n)^{165}Tm
Up	75	5.42(28)×10^{-27}	3.3(5)×10^{-27}	1.90(12)×10^{-27}	1.11(6)×10^{-27}
Up-East	160	2.07(11)×10^{-27}	1.30(20)×10^{-27}	8.4(6)×10^{-28}	4.84(26)×10^{-28}
Up-West	160	1.33(8)×10^{-27}	8.8(14)×10^{-28}	4.7(4)×10^{-28}	3.18(17)×10^{-28}
Up	255	3.22(17)×10^{-27}	2.1(3)×10^{-27}	1.66(11)×10^{-27}	7.8(4)×10^{-28}

* The errors of last digits are given in parentheses.

* The errors shown in these tables do not include the uncertainty of the incident-proton number; it is estimated to be ±10%.

Table 3(b) Reaction rates on the "Down" side of the target vessel

Position Surface	Dist.	Reaction Rates [Nucleus^{-1}Proton^{-1}] ^{115}In(n, n')^{115m}In	^{27}Al(n, α)^{24}Na	^{93}Nb(n, 2n)^{92m}Nb
Down	75	1.08(11)×10^{-26}	5.18(28)×10^{-28}	1.50(8)×10^{-27}
Down	160	9.9(11)×10^{-27}	5.46(29)×10^{-28}	1.48(8)×10^{-27}
Down	255	6.8(7)×10^{-27}	3.77(20)×10^{-28}	9.9(5)×10^{-28}
Down	370	3.9(4)×10^{-27}	1.82(10)×10^{-28}	5.29(28)×10^{-28}
Down	455	1.94(22)×10^{-27}	9.7(5)×10^{-29}	2.72(14)×10^{-28}
Down	750	3.2(4)×10^{-28}	1.48(9)×10^{-29}	4.59(25)×10^{-29}

Position Surface	Dist.	Reaction Rates [Nucleus^{-1}Proton^{-1}] ^{209}Bi(n, 4n)^{206}Bi	^{209}Bi(n, 5n)^{205}Bi	^{209}Bi(n, 6n)^{204}Bi	^{209}Bi(n, 7n)^{203}Bi
Down	75	1.79(9)×10^{-27}	1.37(8)×10^{-27}	8.4(7)×10^{-28}	4.1(4)×10^{-28}
Down	160	1.77(9)×10^{-27}	1.36(8)×10^{-27}	9.2(7)×10^{-28}	4.8(5)×10^{-28}
Down	255	1.40(7)×10^{-27}	1.10(7)×10^{-27}	7.4(6)×10^{-28}	4.3(5)×10^{-28}
Down	370	8.4(4)×10^{-28}	6.5(4)×10^{-28}	4.4(4)×10^{-28}	2.64(27)×10^{-28}
Down	455	4.67(24)×10^{-28}	3.62(23)×10^{-28}	2.61(21)×10^{-28}	1.50(16)×10^{-28}
Down	750	8.3(4)×10^{-29}	6.8(5)×10^{-29}	4.7(4)×10^{-29}	3.2(4)×10^{-29}

Position Surface	Dist.	Reaction Rates [Nucleus^{-1}Proton^{-1}] ^{169}Tm(n, 2n)^{168}Tm	^{169}Tm(n, 3n)^{167}Tm	^{169}Tm(n, 4n)^{166}Tm	^{169}Tm(n, 5n)^{165}Tm
Down	75	6.1(3)×10^{-27}	3.6(6)×10^{-27}	2.17(16)×10^{-27}	1.20(6)×10^{-27}
Down	160	6.0(3)×10^{-27}	3.9(6)×10^{-27}	2.55(19)×10^{-27}	1.39(8)×10^{-27}

* The errors of last digits are given in parentheses.

* The errors shown in these tables do not include the uncertainty of the incident-proton number; it is estimated to be ±10%.

Table 3(c) Reaction rates on the "East" side of the target vessel

Position Surface	Dist.	Reaction Rates [Nucleus^{-1}Proton^{-1}] ^{115}In(n, n')^{115m}In	^{27}Al(n, α)^{24}Na	^{93}Nb(n, 2n)^{92m}Nb
East	75	$1.28(14)\times10^{-27}$	$4.53(25)\times10^{-29}$	$1.40(7)\times10^{-28}$
East	160	$1.04(11)\times10^{-27}$	$3.95(22)\times10^{-29}$	$1.24(7)\times10^{-28}$
East	255	$7.8(8)\times10^{-28}$	$2.67(16)\times10^{-29}$	$8.4(4)\times10^{-29}$
East	370	$4.9(5)\times10^{-28}$	$1.73(10)\times10^{-29}$	$4.90(26)\times10^{-29}$
East	455	$3.7(4)\times10^{-28}$	$1.08(7)\times10^{-29}$	$3.19(17)\times10^{-29}$
East	750	$1.20(15)\times10^{-28}$	$3.98(27)\times10^{-30}$	$9.2(5)\times10^{-30}$

Position Surface	Dist.	Reaction Rates [Nucleus^{-1}Proton^{-1}] ^{209}Bi(n, 4n)^{206}Bi	^{209}Bi(n, 5n)^{205}Bi	^{209}Bi(n, 6n)^{204}Bi	^{209}Bi(n, 7n)^{203}Bi
East	75	$1.96(10)\times10^{-28}$	$1.36(9)\times10^{-28}$	$8.3(7)\times10^{-29}$	$3.3(5)\times10^{-29}$
East	160	$1.89(10)\times10^{-28}$	$1.33(9)\times10^{-28}$	$8.7(7)\times10^{-29}$	$4.5(5)\times10^{-29}$
East	255	$1.35(7)\times10^{-28}$	$9.7(6)\times10^{-29}$	$6.7(6)\times10^{-29}$	$4.4(5)\times10^{-29}$
East	370	$8.3(4)\times10^{-29}$	$6.1(4)\times10^{-29}$	$4.7(4)\times10^{-29}$	$2.3(3)\times10^{-29}$
East	455	$5.59(29)\times10^{-29}$	$4.05(28)\times10^{-29}$	$2.94(27)\times10^{-29}$	$1.55(25)\times10^{-29}$
East	750	$1.80(9)\times10^{-29}$	$1.38(10)\times10^{-29}$	$1.05(10)\times10^{-29}$	$3.51(99)\times10^{-30}$

Position Surface	Dist.	Reaction Rates [Nucleus^{-1}Proton^{-1}] ^{169}Tm(n, 2n)^{168}Tm	^{169}Tm(n, 3n)^{167}Tm	^{169}Tm(n, 4n)^{166}Tm	^{169}Tm(n, 5n)^{165}Tm
East	75	$6.0(3)\times10^{-28}$	$3.8(6)\times10^{-28}$	$2.10(19)\times10^{-28}$	$1.24(7)\times10^{-28}$
East	160	$5.1(3)\times10^{-28}$	$3.4(5)\times10^{-28}$	$2.01(19)\times10^{-28}$	$1.25(7)\times10^{-28}$

* The errors of last digits are given in parentheses.

* The errors shown in these tables do not include the uncertainty of the incident-proton number; it is estimated to be ±10%.

Table 3(d) Reaction rates on the "West" side of the target vessel

Position Surface	Dist.	Reaction Rates [Nucleus^{-1}Proton^{-1}] ^{115}In(n, n')^{115m}In	^{27}Al(n, α)^{24}Na	^{93}Nb(n, 2n)^{92m}Nb
West	75	9.5(10)×10^{-28}	3.39(19)×10^{-29}	1.01(5)×10^{-28}
West	160	9.10(10)×10^{-28}	3.03(17)×10^{-29}	8.9(5)×10^{-29}
West	255	6.1(7)×10^{-28}	2.26(13)×10^{-29}	6.3(3)×10^{-29}
West	370	3.4(4)×10^{-28}	1.38(8)×10^{-29}	3.65(20)×10^{-29}
West	455	2.04(25)×10^{-28}	9.4(6)×10^{-30}	2.43(13)×10^{-29}
West	750	8.5(11)×10^{-29}	4.08(28)×10^{-30}	7.9(5)×10^{-30}

Position Surface	Dist.	Reaction Rates [Nucleus^{-1}Proton^{-1}] ^{209}Bi(n, 4n)^{206}Bi	^{209}Bi(n, 5n)^{205}Bi	^{209}Bi(n, 6n)^{204}Bi	^{209}Bi(n, 7n)^{203}Bi
West	75	1.56(8)×10^{-28}	9.6(6)×10^{-29}	7.4(6)×10^{-29}	3.2(4)×10^{-29}
West	160	1.38(7)×10^{-28}	9.4(6)×10^{-29}	6.5(5)×10^{-29}	3.4(4)×10^{-29}
West	255	1.05(5)×10^{-28}	7.7(5)×10^{-29}	5.8(5)×10^{-29}	3.1(4)×10^{-29}
West	370	6.7(3)×10^{-29}	5.0(3)×10^{-29}	3.5 (3)×10^{-29}	1.66(27)×10^{-29}
West	455	4.45(23)×10^{-29}	3.37(22)×10^{-29}	2.22(18)×10^{-29}	1.66(19)×10^{-29}
West	750	1.64(8)×10^{-29}	1.24(8)×10^{-29}	8.1(6)×10^{-30}	4.7(5)×10^{-30}

Position Surface	Dist.	Reaction Rates [Nucleus^{-1}Proton^{-1}] ^{169}Tm(n, 2n)^{168}Tm	^{169}Tm(n, 3n)^{167}Tm	^{169}Tm(n, 4n)^{166}Tm	^{169}Tm(n, 5n)^{165}Tm
West	75	4.29(25)×10^{-28}	2.9(4)×10^{-28}	1.45(14)×10^{-28}	9.4(5)×10^{-29}
West	160	3.91(24)×10^{-28}	2.6(4)×10^{-28}	1.99(18)×10^{-28}	9.3(5)×10^{-29}

* The errors of last digits are given in parentheses.
* The errors shown in these tables do not include the uncertainty of the incident-proton number; it is estimated to be ±10%.

Table 3(e) Reaction rates on the "Front" side of the target vessel

Position Surface	Dist.	Reaction Rates [Nucleus^{-1}Proton^{-1}] ^{115}In(n, n')^{115m}In	^{27}Al(n, α)^{24}Na	^{93}Nb(n, 2n)^{92m}Nb
Front	0	1.28(14)×10^{-27}	4.35(24)×10^{-29}	1.15(6)×10^{-28}

Position Surface	Dist.	Reaction Rates [Nucleus^{-1}Proton^{-1}] ^{209}Bi(n, 4n)^{206}Bi	^{209}Bi(n, 5n)^{205}Bi	^{209}Bi(n, 6n)^{204}Bi	^{209}Bi(n, 7n)^{203}Bi
Front	0	1.53(8)×10^{-28}	1.06(7)×10^{-28}	7.1(6)×10^{-29}	3.1(5)×10^{-29}

* The errors of last digits are given in parentheses.
* The errors shown in these tables do not include the uncertainty of the incident-proton number; it is estimated to be ±10%.

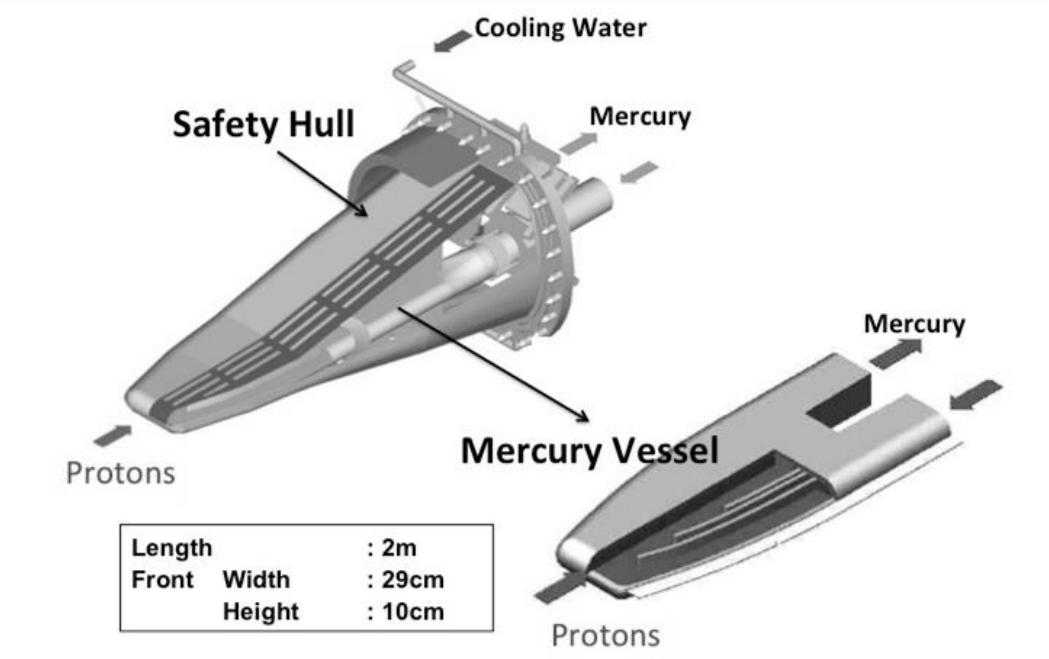

Fig. 1 Configuration of the mercury target. The mercury vessel is covered by the safety hull with a cooling water channel. Helium gas is contained in the intermediate layer between the mercury target and the safety hull. The main constructional material is SUS316L.

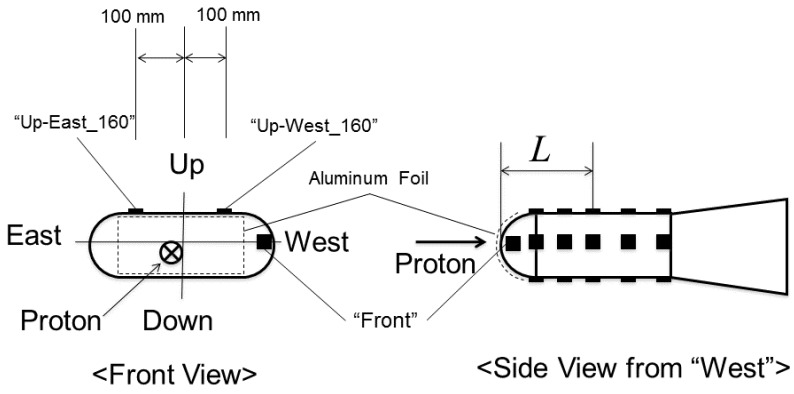

Fig. 2 Activation foils were set on the surface of the mercury target vessel at the positions labeled as "Surface-Length": the "Surfaces" were labeled as "Up", "Down", "East" and "West", and the "Length" means the distances between the vessel top and the sample positions in millimeters. For example, the label of "East-160" means the position at 160-mm distance from the vessel top on the surface of the east side. The foils labeled as "Up-East_160" and "Up-West_160" were pasted on the off-center positions because the position corresponding to "Up_160" was just on the reflecting mirror of laser beam for monitoring the vibration induced on the vessel surface by the pulsed proton beam. The "Front" foils were set on the beam-incident surface. The beam-incident front was covered by the aluminum foil for measurement of the incident proton beam profile.

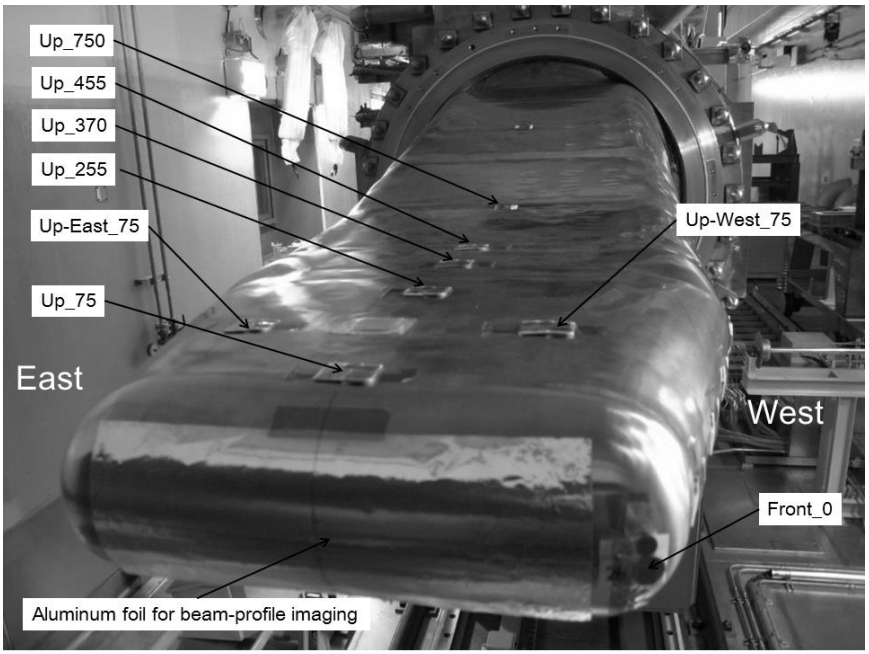

Fig. 3 Photos of sample setting. The labels such as "Up_75" show the sample positions: the "Up_75" means the samples on the "Up"-side at 75-mm distance from the vessel top.

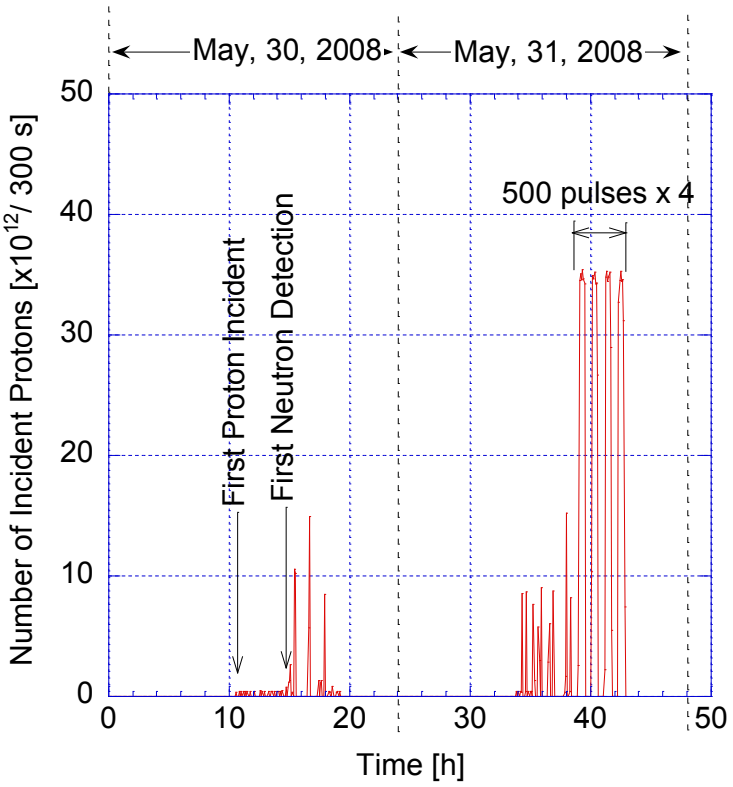

Fig. 4 History of the incident proton-beam intensity during the first beam run on May 30 and 31.

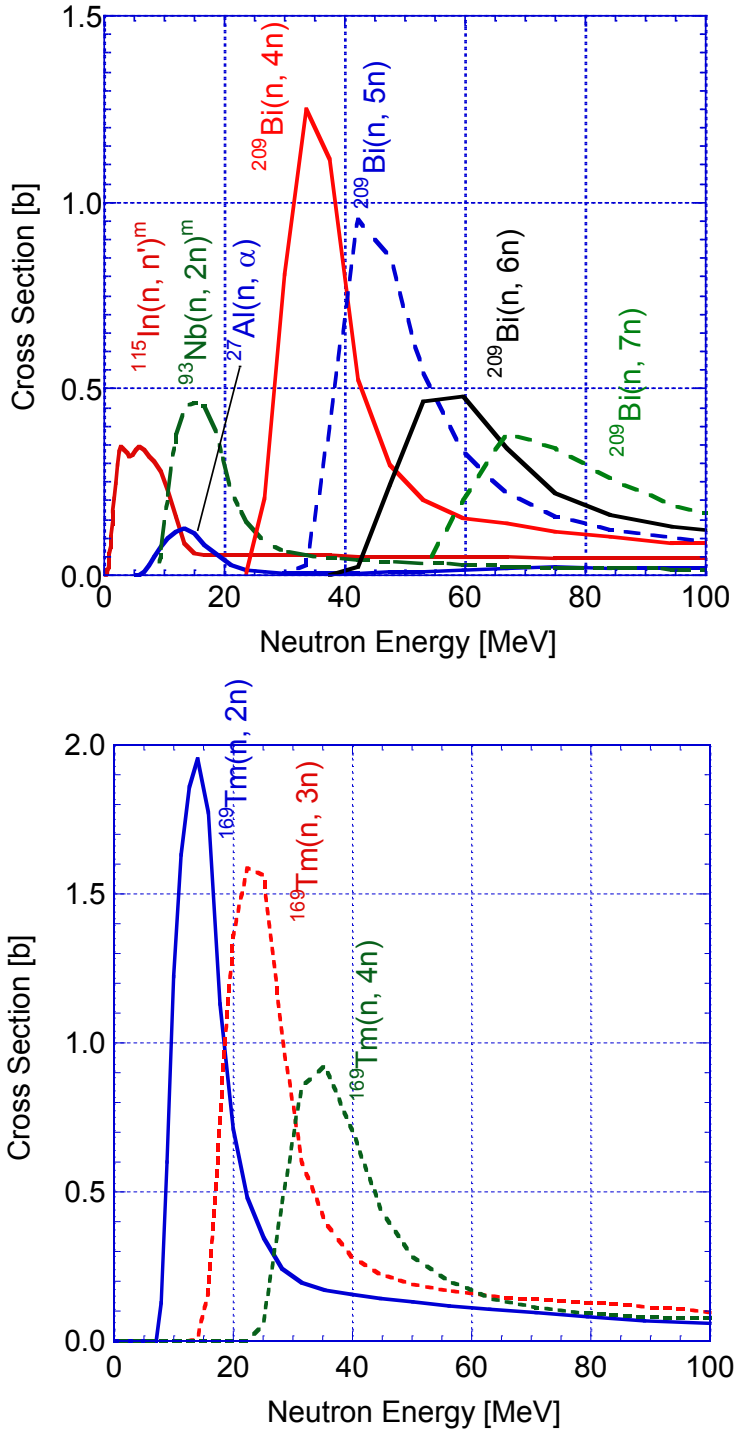

Fig. 5 Cross-section curves of the neutron induced reactions used in this experiment.

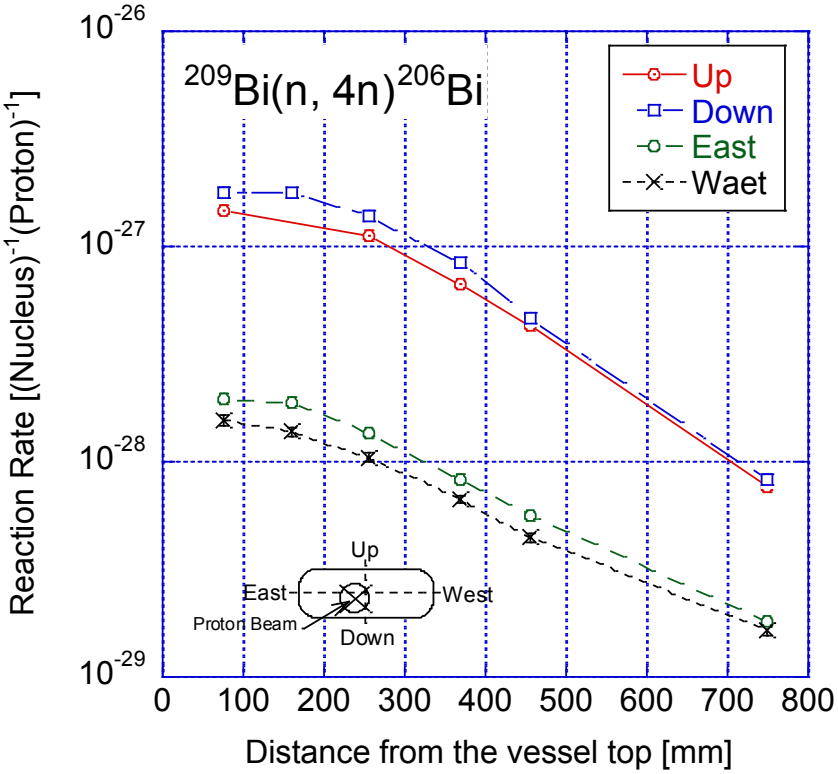

Fig. 6 Reaction rate distributions of ^{209}Bi(n, 4n)^{206}Bi on every sides of the mercury vessel. The reaction rates of "Down" are larger than the those of "Up", and "East" is larger than "West"; these results show that the center of the proton beam profile was shifted to "Down"-"East" for the target center as shown in the lower part of the figure. The shift of the proton beam center corresponds to the result of the activation of the aluminum foil pasted on the beam incident surface of the mercury target vessel shown in Fig. 7.

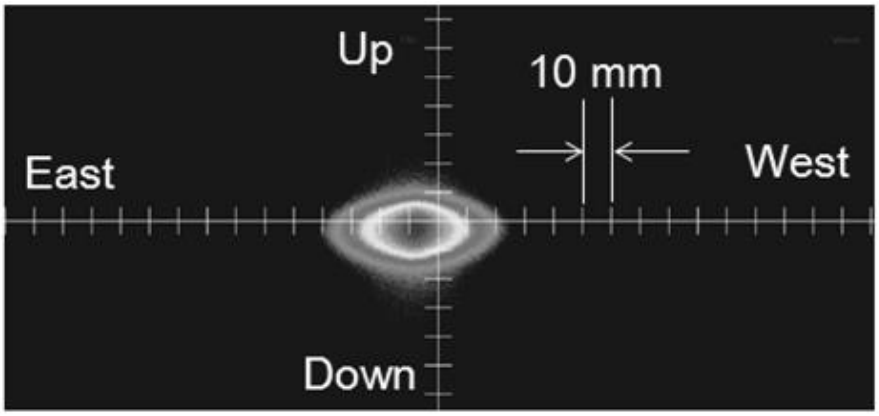

Fig. 7 Image of the activation distribution of the aluminum foil pasted on the beam-incident front of the mercury target vessel. The image corresponded to the proton beam profile accumulated during the first beam-run. The profile center was shifted to 3 mm-down and 7 mm east from the target center.

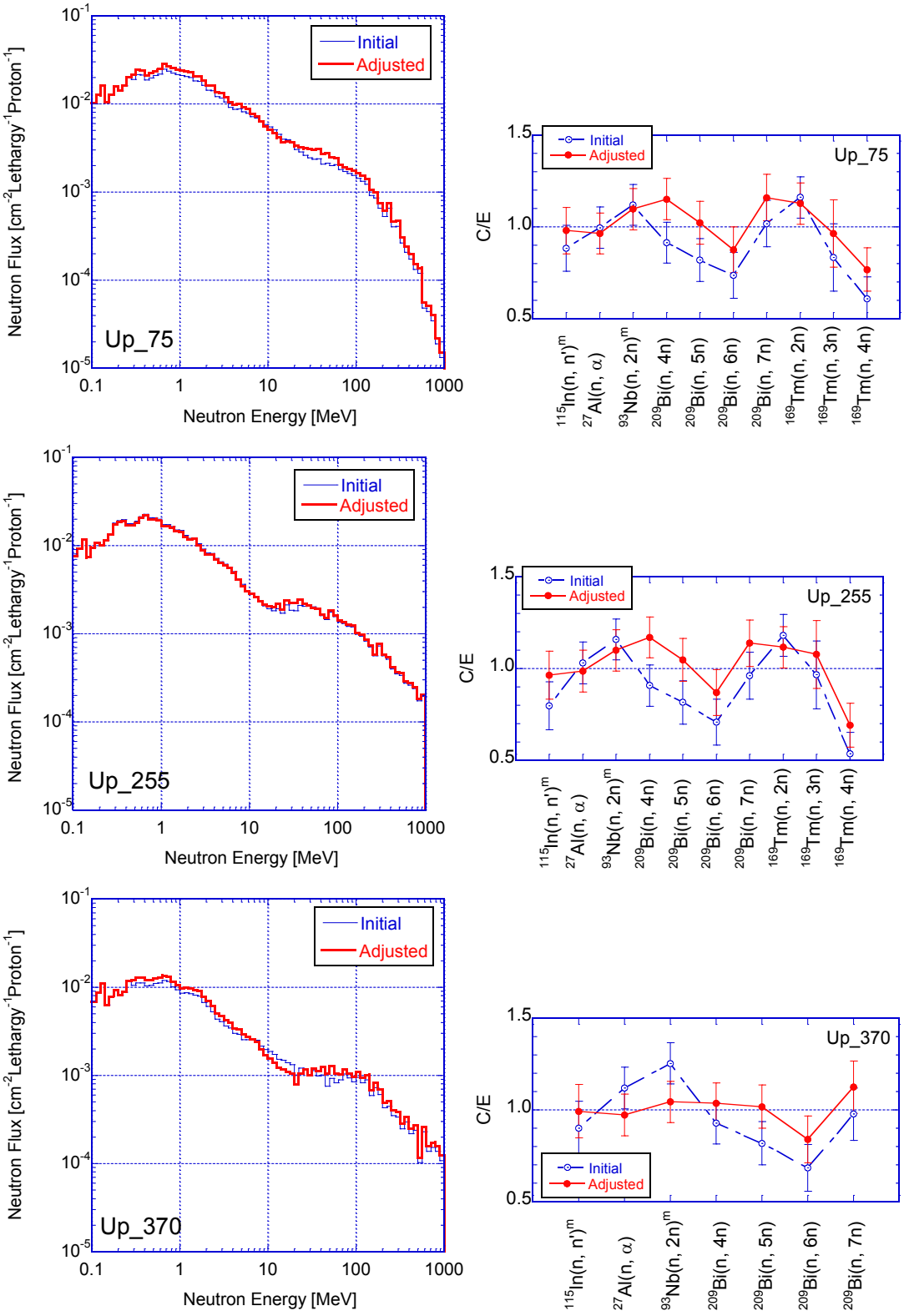

Fig. 8(a) Neutron spectra and the C/E-values of the reaction rates on the "Up" positions. The "unfolded" neutron spectra were deduced with unfolding method from the "initial" spectra estimated by the calculation using PHITS code. The values of C/E mean the ratios of the reaction rates deduced from the neutron spectrum ("initial" and "unfolded") to the experimental reaction-rate data.

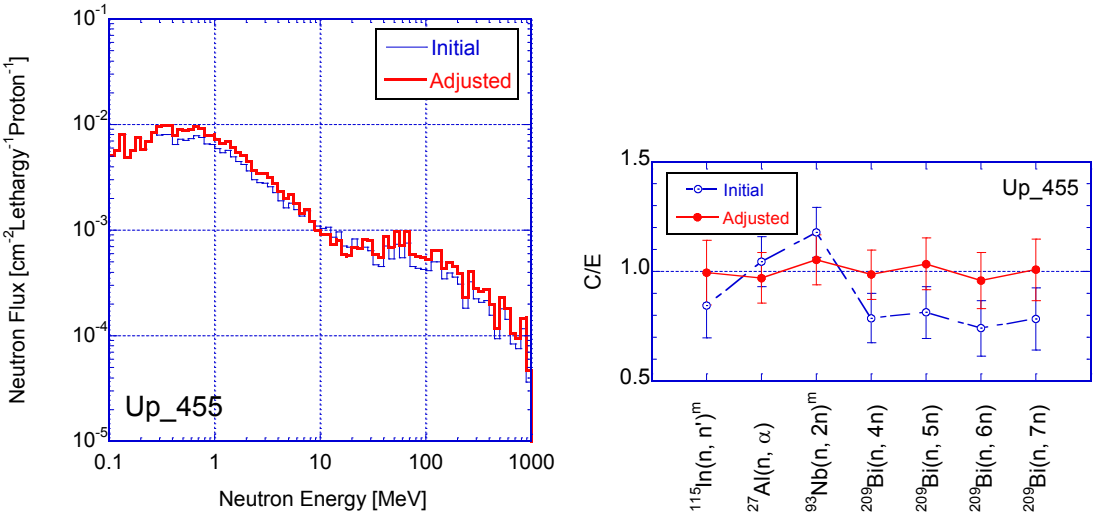

Fig. 8(a) (Continued)

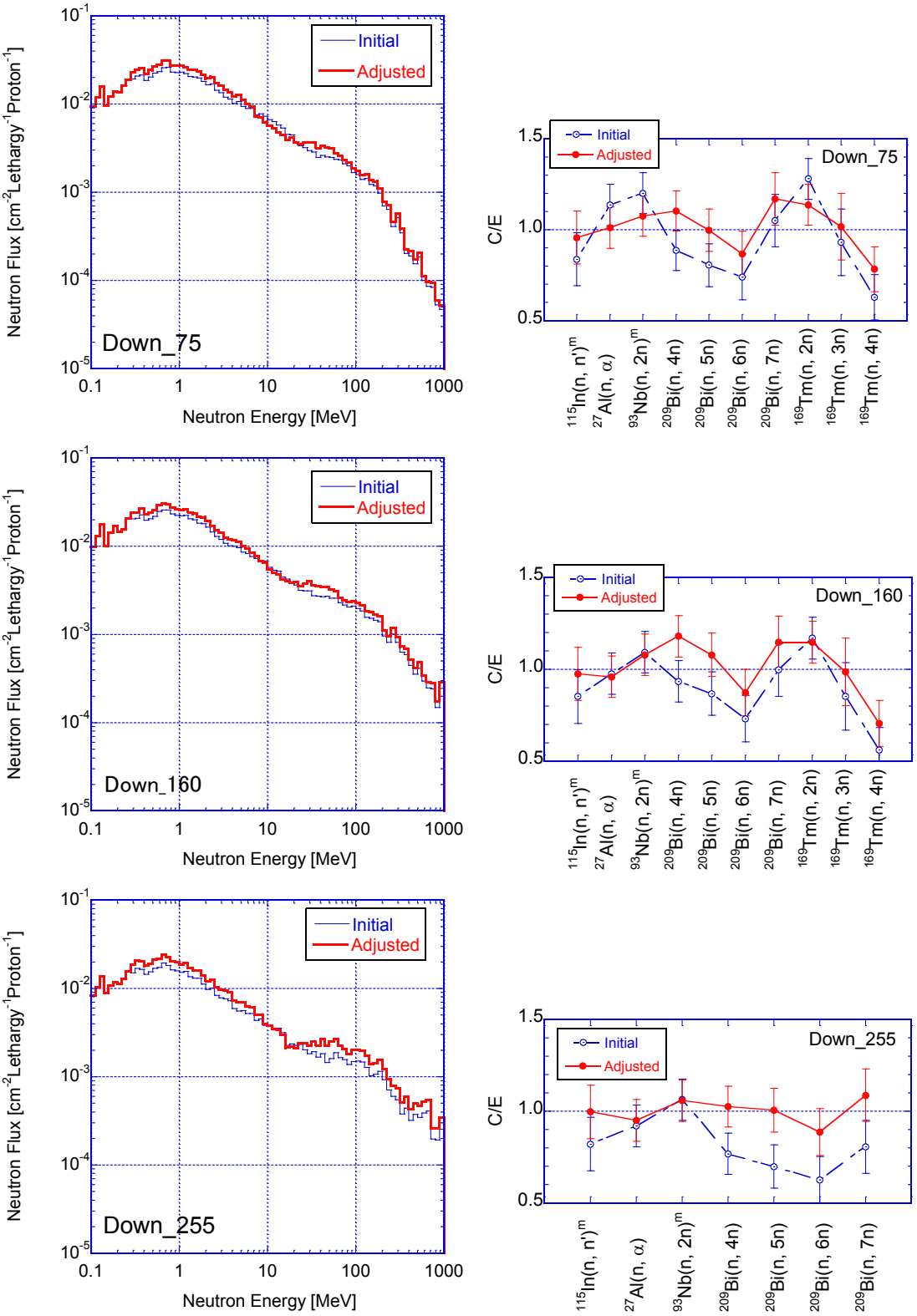

Fig. 8(b) Neutron spectra and the C/E-values of the reaction rates on the "Down" positions.

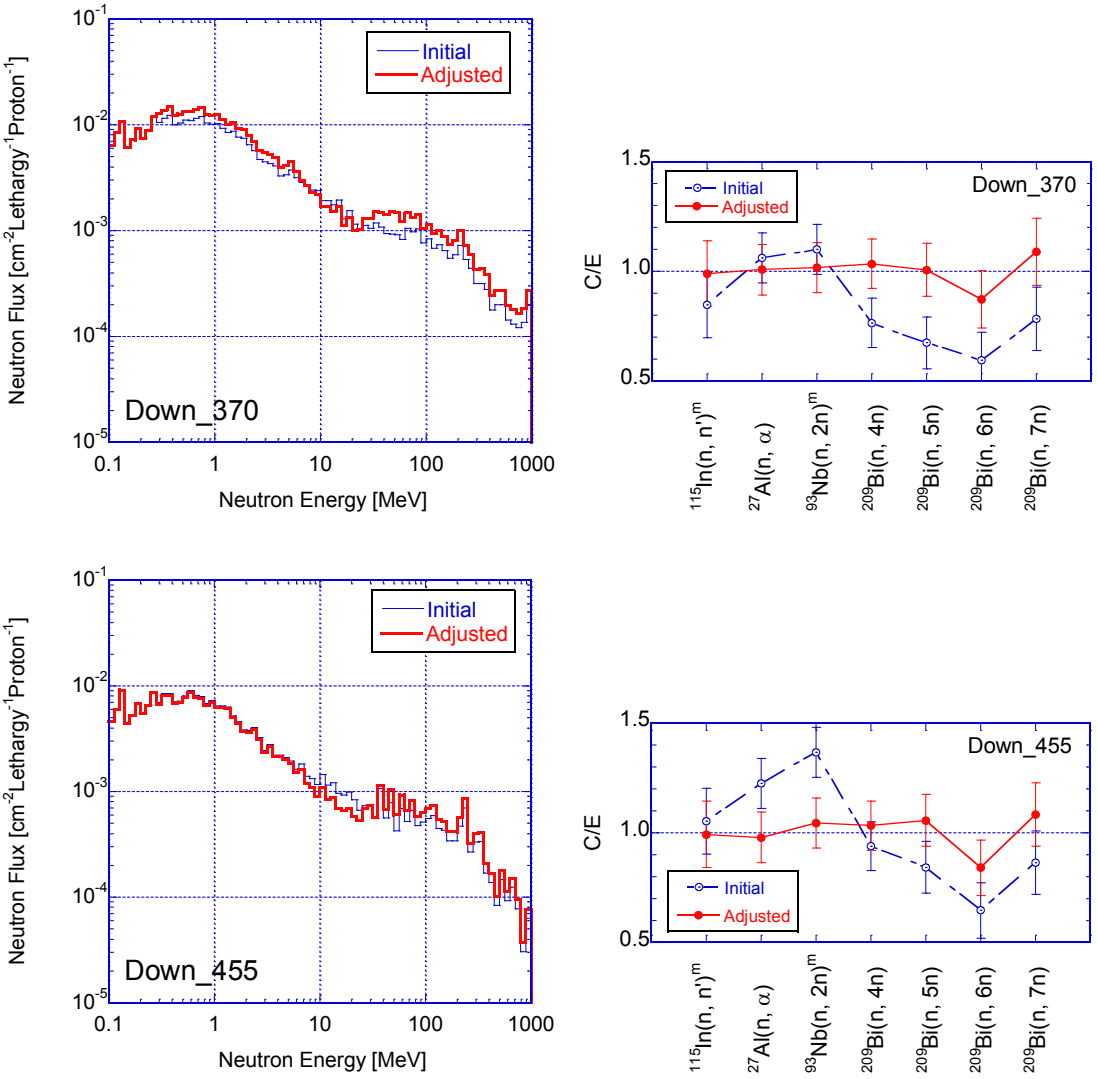

Fig. 8(b) Neutron spectra and the C/E-values of the reaction rates on the "Down" positions. (Continued)

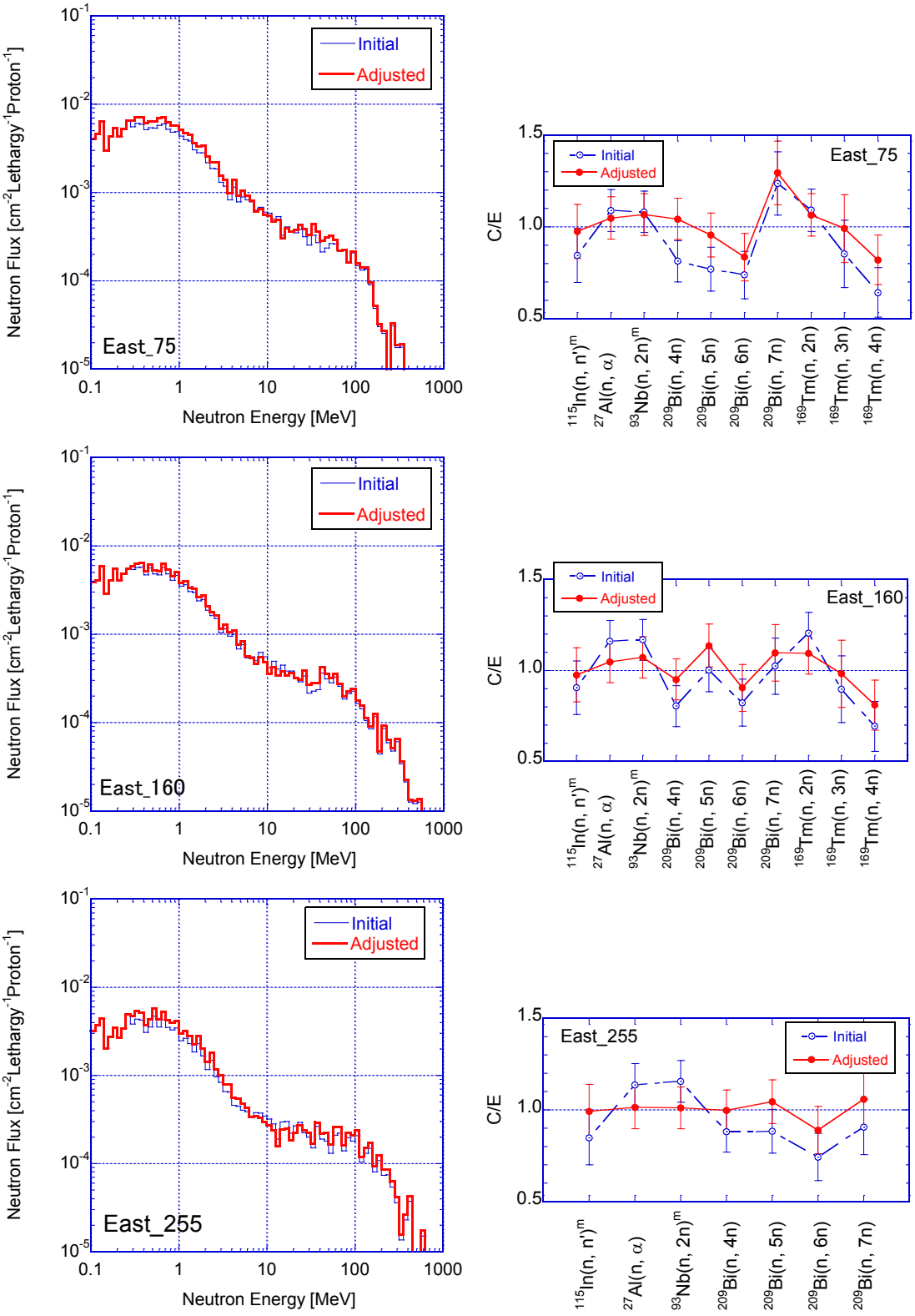

Fig. 8(c) Neutron spectra and the C/E-values of the reaction rates on the "East" positions.

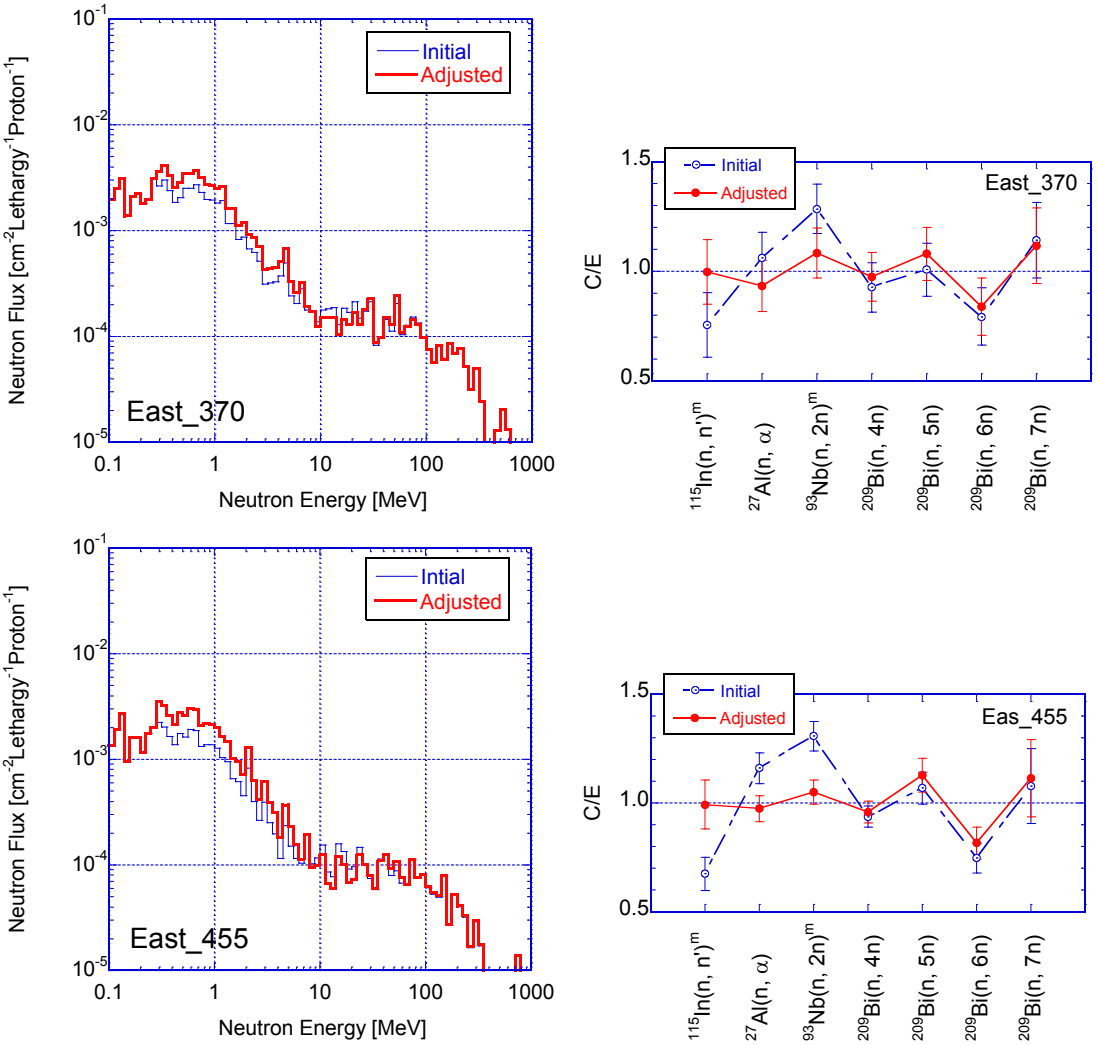

Fig. 8(c) Neutron spectra and the C/E-values of the reaction rates on the "East" positions. (Continued)

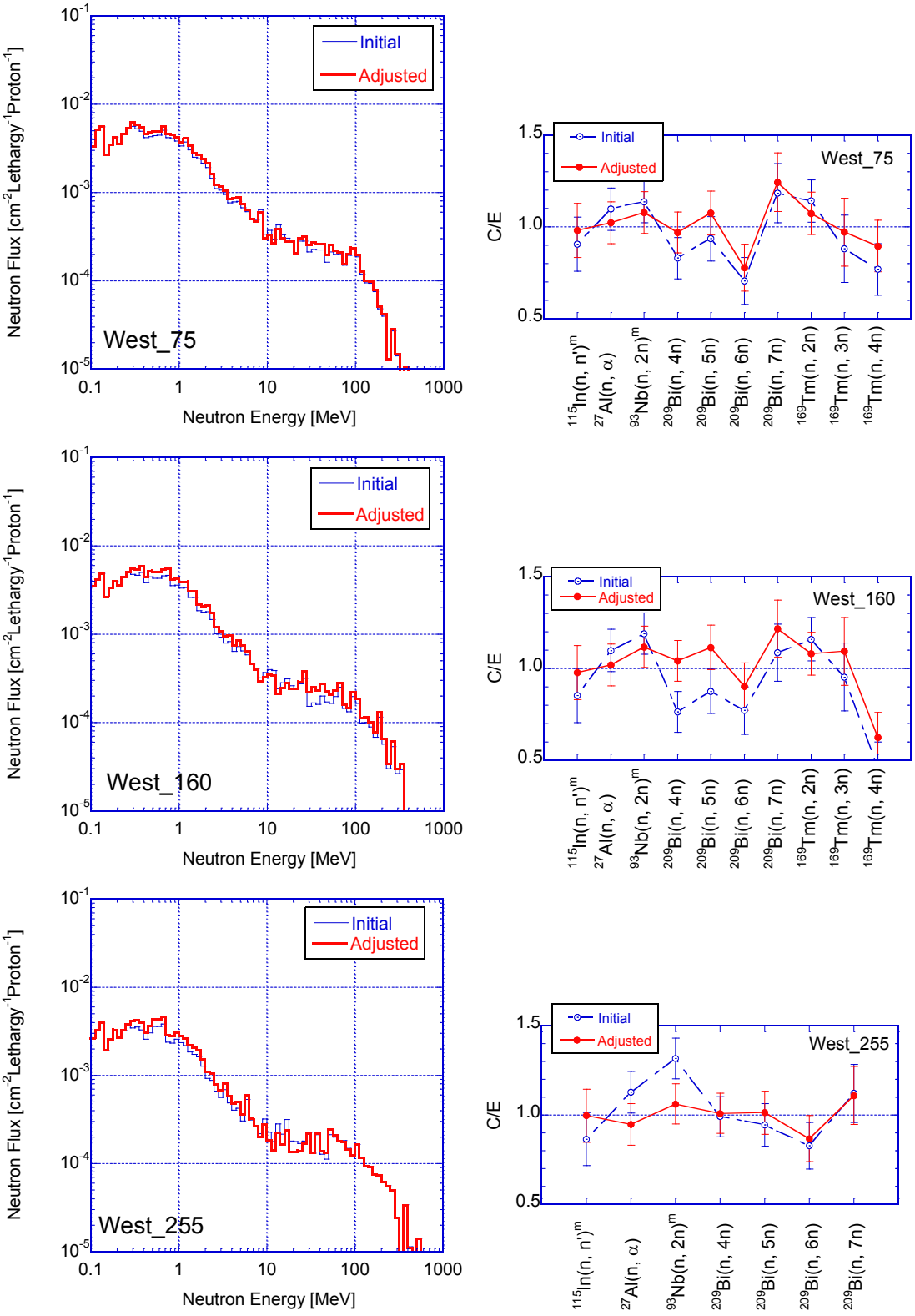

Fig. 8(d) Neutron spectra and the C/E-values of the reaction rates on the "West" positions.

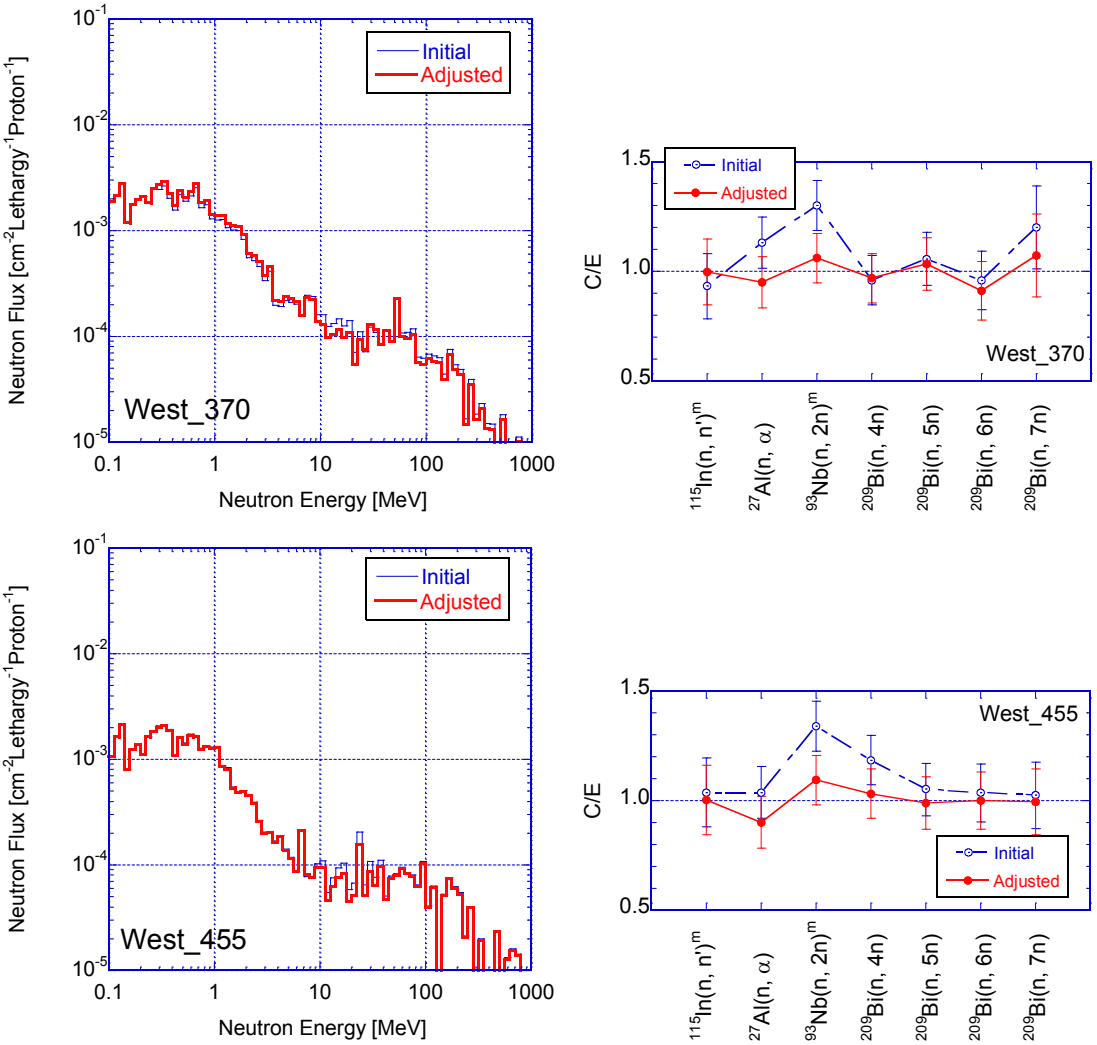

Fig. 8(d) Neutron spectra and the C/E-values of the reaction rates on the "West" positions. (Continued)

Appendix A Measurement of ^{24}Na Induced in Aluminum Foils using an Imaging Plate

After the proton-beam operation, we need to measure more than 100 activation foils using only one HPGe detector, and the half-lives of some radioactive products to be measured is short: that of ^{115m}In (4.5 h) is the shortest. In order to measure all the activation foils efficiently without sacrificing the statistics of gamma-ray counting, we also utilize an imaging plate (IP).

In order to use the IP for radioactivity determination, it is required that only a single radioactive nuclide remains as residual in an activation foils. The main products of aluminum foils for high-energy neutron irradiation are ^{24}Na ($T_{1/2}$=15 h) produced via ^{27}Al(n, α)^{24}Na reaction and ^{27}Mg ($T_{1/2}$=9.6 m) via ^{27}Al(n, p)^{27}Mg reaction. After considerable cooling time, the ^{24}Na radioactivity only remains as residual.

In the measurement, all of the aluminum foils was placed on an IP. Exposing and analyzing the IP, the Imaging Plate Luminescence (PSL), corresponding to the relative intensities of ^{24}Na, were obtained for each foil at once. For getting the absolute activities of ^{24}Na, some of the aluminum foils was measured with the HPGe detector. The relation between ^{24}Na activity and PSL was drawn in Fig. A1, which shows good linearity between them. We estimated that the radioactivity determination with IP method contains ±6% uncertainty.

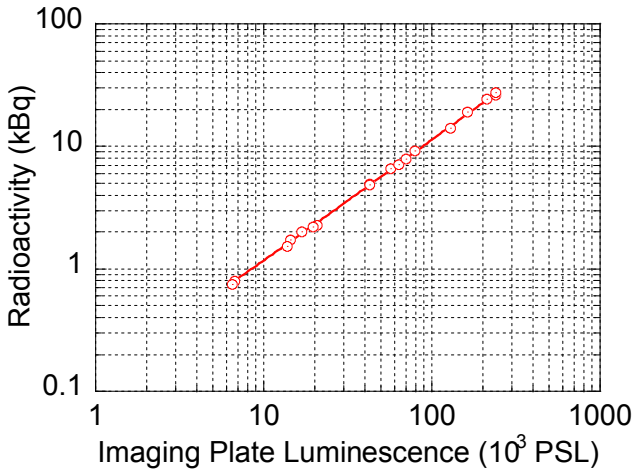

Fig. A1 Relation between the imaging plate luminescence (PSL) and activities of ^{24}Na induced in the aluminum foils.

Appendix B Deduction of the Irradiation Factor F_{irr} when the Proton Beam Intensity is Constant in Time

The irradiation factor in this work was defined as follows:

$$F_{irr} = \sum_{n=0}^{N-1} I_p(t_n)\left(1 - e^{-\lambda \Delta t}\right) e^{-\lambda\{t_f - (t_n + \Delta t)\}} \quad , \tag{B1}$$

where

Δt: Sampling time,

t_i: Irradiation start time,

t_f: Irradiation termination time,

$I_p(t_n)$: Number of incident protons per second averaged between t_n and $t_n+\Delta t$.

In addition, we set $N = (t_f - t_i)/\Delta t$ and $t_n = t_i + n\Delta t$. The mathematical model of this equation is shown in Fig. B1. We rewrite the equation using $T = t_f - t_i$ as

$$F_{irr} = \sum_{n=0}^{N-1} I_p(t_n)\left(1 - e^{-\lambda \Delta t}\right) e^{-\lambda T} e^{\lambda \Delta t (n+1)} \quad . \tag{B2}$$

Suppose that $I_p(t_n)=I_p$ is constant, the equation (B2) can be written as

$$F_{irr}^{c} = I_p\left(1 - e^{-\lambda \Delta t}\right) e^{-\lambda T} \sum_{n=0}^{N-1} e^{\lambda \Delta t (n+1)} \quad . \tag{B3}$$

Here we change the notation F_{irr} to F_{irr}^{c}. Then,[vi]

$$\begin{aligned} \sum_{n=0}^{N-1} e^{\lambda \Delta t (n+1)} &= e^{\lambda \Delta T} + e^{\lambda \cdot 2\Delta T} + \cdots + e^{\lambda \cdot N \Delta t} \\ &= \frac{e^{\lambda \Delta t} - e^{\lambda (N+1) \Delta t}}{1 - e^{\lambda \Delta t}} = \frac{1 - e^{\lambda N \Delta t}}{e^{-\lambda \Delta t} - 1} \\ &= \frac{e^{\lambda T} - 1}{1 - e^{-\lambda \Delta t}} \end{aligned} \quad . \tag{B4}$$

Therefore, we get

$$F_{irr}^{c} = I_p\left(1 - e^{-\lambda \Delta t}\right) e^{-\lambda T} \frac{e^{\lambda T} - 1}{1 - e^{-\lambda \Delta t}} = I_p(1 - e^{-\lambda T}) \quad . \tag{B5}$$

In Fig. B2, the ratios of F_{irr}^{c} to F_i are shown as a function of the half-lives of radioactive products. In the calculation of F_{irr}^{c}, the values of I_p and T were set to be 8.4×10^{14} and 3.8 hours corresponding to the factor for the dedicated run on May 31. The graph shows that the contribution of the conditioning run on May 30 to the radioactivity productions was larger as the half-lives of the products were getting longer.

[vi] $S = a + a^2 + \cdots + a^N = (a - a^{N+1})/(1 - a)$

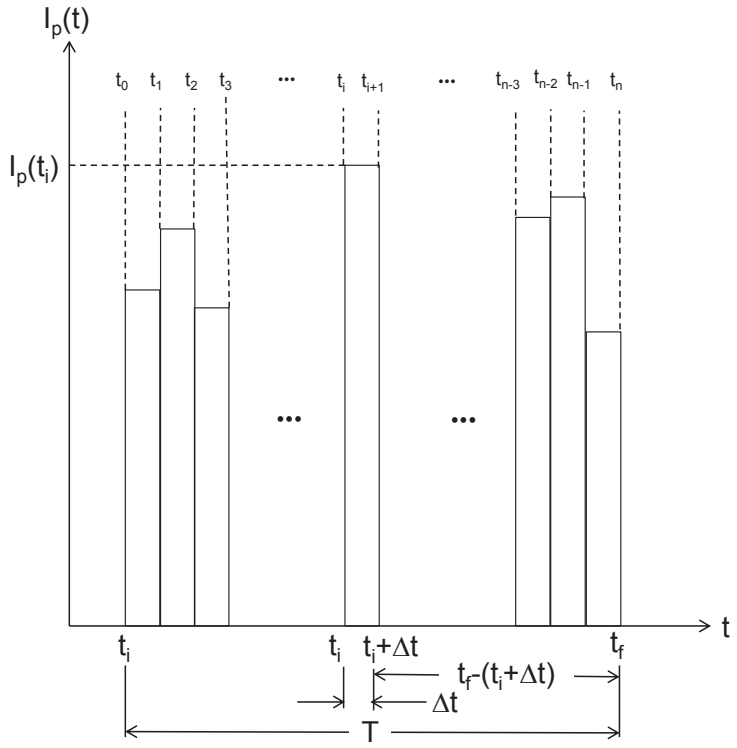

Fig. B1 Mathematical model for deduction of the equation (A1).

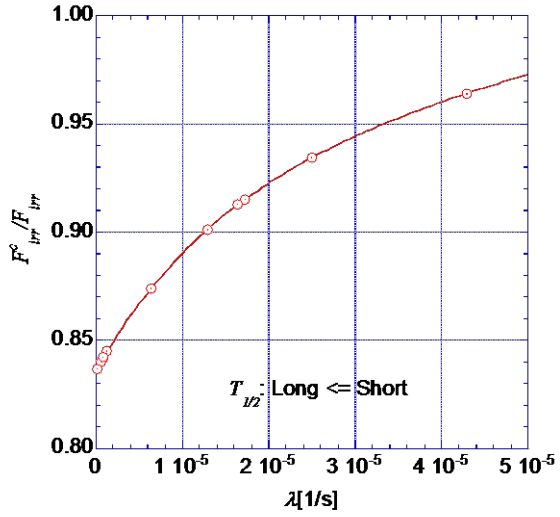

Fig. B2 The values of F_{irr}^{c}/F_{irr} as a function of half-lives of the products

国際単位系（SI）

表１．SI 基本単位

基本量	SI 基本単位	
	名称	記号
長さ	メートル	m
質量	キログラム	kg
時間	秒	s
電流	アンペア	A
熱力学温度	ケルビン	K
物質量	モル	mol
光度	カンデラ	cd

表２．基本単位を用いて表されるSI組立単位の例

組立量	SI 組立単位	
	名称	記号
面積	平方メートル	m^2
体積	立方メートル	m^3
速さ，速度	メートル毎秒	m/s
加速度	メートル毎秒毎秒	m/s^2
波数	毎メートル	m^{-1}
密度，質量密度	キログラム毎立方メートル	kg/m^3
面積密度	キログラム毎平方メートル	kg/m^2
比体積	立方メートル毎キログラム	m^3/kg
電流密度	アンペア毎平方メートル	A/m^2
磁界の強さ	アンペア毎メートル	A/m
量濃度(a)，濃度	モル毎立方メートル	mol/m^3
質量濃度	キログラム毎立方メートル	kg/m^3
輝度	カンデラ毎平方メートル	cd/m^2
屈折率(b)	（数字の） 1	1
比透磁率(b)	（数字の） 1	1

(a) 量濃度（amount concentration）は臨床化学の分野では物質濃度（substance concentration）ともよばれる。
(b) これらは無次元量あるいは次元１をもつ量であるが、そのことを表す単位記号である数字の１は通常は表記しない。

表３．固有の名称と記号で表されるSI組立単位

組立量	SI 組立単位			
	名称	記号	他のSI単位による表し方	SI基本単位による表し方
平面角	ラジアン(b)	rad	1 (b)	m/m
立体角	ステラジアン(b)	sr(c)	1 (b)	m^2/m^2
周波数	ヘルツ(d)	Hz		s^{-1}
力	ニュートン	N		m kg s^{-2}
圧力，応力	パスカル	Pa	N/m^2	m^{-1} kg s^{-2}
エネルギー，仕事，熱量	ジュール	J	N m	m^2 kg s^{-2}
仕事率，工率，放射束	ワット	W	J/s	m^2 kg s^{-3}
電荷，電気量	クーロン	C		s A
電位差（電圧），起電力	ボルト	V	W/A	m^2 kg s^{-3} A^{-1}
静電容量	ファラド	F	C/V	m^{-2} kg^{-1} s^4 A^2
電気抵抗	オーム	Ω	V/A	m^2 kg s^{-3} A^{-2}
コンダクタンス	ジーメンス	S	A/V	m^{-2} kg^{-1} s^3 A^2
磁束	ウエーバ	Wb	Vs	m^2 kg s^{-2} A^{-1}
磁束密度	テスラ	T	Wb/m^2	kg s^{-2} A^{-1}
インダクタンス	ヘンリー	H	Wb/A	m^2 kg s^{-2} A^{-2}
セルシウス温度	セルシウス度(e)	℃		K
光束	ルーメン	lm	cd sr(c)	cd
照度	ルクス	lx	lm/m^2	m^{-2} cd
放射性核種の放射能(f)	ベクレル(d)	Bq		s^{-1}
吸収線量，比エネルギー分与，カーマ	グレイ	Gy	J/kg	m^2 s^{-2}
線量当量，周辺線量当量，方向性線量当量，個人線量当量	シーベルト(g)	Sv	J/kg	m^2 s^{-2}
酸素活性	カタール	kat		s^{-1} mol

(a)SI接頭語は固有の名称と記号を持つ組立単位と組み合わせても使用できる。しかし接頭語を付した単位はもはやコヒーレントではない。
(b)ラジアンとステラジアンは数字の１に対する単位の特別な名称で、量についての情報をつたえるために使われる。実際には、使用する時には記号radおよびsrが用いられるが、習慣として組立単位としての記号である数字の１は明示されない。
(c)測光学ではステラジアンという名称と記号srを単位の表し方の中に、そのまま維持している。
(d)ヘルツは周期現象についてのみ、ベクレルは放射性核種の統計的過程についてのみ使用される。
(e)セルシウス度はケルビンの特別な名称で、セルシウス温度を表すために使用される。セルシウス度とケルビンの単位の大きさは同一である。したがって、温度差や温度間隔を表す数値はどちらの単位で表しても同じである。
(f)放射性核種の放射能（activity referred to a radionuclide）は、しばしば誤った用語で"radioactivity"と記される。
(g)単位シーベルト（PV,2002,70,205）についてはCIPM勧告2（CI-2002）を参照。

表４．単位の中に固有の名称と記号を含むSI組立単位の例

組立量	SI 組立単位		
	名称	記号	SI 基本単位による表し方
粘度	パスカル秒	Pa s	m^{-1} kg s^{-1}
力のモーメント	ニュートンメートル	N m	m^2 kg s^{-2}
表面張力	ニュートン毎メートル	N/m	kg s^{-2}
角速度	ラジアン毎秒	rad/s	m m^{-1} s^{-1}=s^{-1}
角加速度	ラジアン毎秒毎秒	rad/s^2	m m^{-1} s^{-2}=s^{-2}
熱流密度，放射照度	ワット毎平方メートル	W/m^2	kg s^{-3}
熱容量，エントロピー	ジュール毎ケルビン	J/K	m^2 kg s^{-2} K^{-1}
比熱容量，比エントロピー	ジュール毎キログラム毎ケルビン	J/(kg K)	m^2 s^{-2} K^{-1}
比エネルギー	ジュール毎キログラム	J/kg	m^2 s^{-2}
熱伝導率	ワット毎メートル毎ケルビン	W/(m K)	m kg s^{-3} K^{-1}
体積エネルギー	ジュール毎立方メートル	J/m^3	m^{-1} kg s^{-2}
電界の強さ	ボルト毎メートル	V/m	m kg s^{-3} A^{-1}
電荷密度	クーロン毎立方メートル	C/m^3	m^{-3} s A
表面電荷	クーロン毎平方メートル	C/m^2	m^{-2} s A
電束密度，電気変位	クーロン毎平方メートル	C/m^2	m^{-2} s A
誘電率	ファラド毎メートル	F/m	m^{-3} kg^{-1} s^4 A^2
透磁率	ヘンリー毎メートル	H/m	m kg s^{-2} A^{-2}
モルエネルギー	ジュール毎モル	J/mol	m^2 kg s^{-2} mol^{-1}
モルエントロピー，モル熱容量	ジュール毎モル毎ケルビン	J/(mol K)	m^2 kg s^{-2} K^{-1} mol^{-1}
照射線量（X線及びγ線）	クーロン毎キログラム	C/kg	kg^{-1} s A
吸収線量率	グレイ毎秒	Gy/s	m^2 s^{-3}
放射強度	ワット毎ステラジアン	W/sr	m^4 m^{-2} kg s^{-3}=m^2 kg s^{-3}
放射輝度	ワット毎平方メートル毎ステラジアン	$W/(m^2$ sr)	m^2 m^{-2} kg s^{-3}=kg s^{-3}
酵素活性濃度	カタール毎立方メートル	kat/m^3	m^{-3} s^{-1} mol

表５．SI 接頭語

乗数	名称	記号	乗数	名称	記号
10^{24}	ヨタ	Y	10^{-1}	デシ	d
10^{21}	ゼタ	Z	10^{-2}	センチ	c
10^{18}	エクサ	E	10^{-3}	ミリ	m
10^{15}	ペタ	P	10^{-6}	マイクロ	μ
10^{12}	テラ	T	10^{-9}	ナノ	n
10^{9}	ギガ	G	10^{-12}	ピコ	p
10^{6}	メガ	M	10^{-15}	フェムト	f
10^{3}	キロ	k	10^{-18}	アト	a
10^{2}	ヘクト	h	10^{-21}	ゼプト	z
10^{1}	デカ	da	10^{-24}	ヨクト	y

表６．SIに属さないが、SIと併用される単位

名称	記号	SI 単位による値
分	min	1 min=60 s
時	h	1 h =60 min=3600 s
日	d	1 d=24 h=86 400 s
度	°	1°=(π/180) rad
分	’	1’=(1/60)°=(π/10 800) rad
秒	”	1”=(1/60)’=(π/648 000) rad
ヘクタール	ha	1 ha=1 hm^2=10^4m^2
リットル	L, l	1 L=1 l=1 dm^3=10^3cm^3=$10^{-3}m^3$
トン	t	1 t=10^3 kg

表７．SIに属さないが、SIと併用される単位で、SI単位で表される数値が実験的に得られるもの

名称	記号	SI 単位で表される数値
電子ボルト	eV	1 eV=1.602 176 53(14)×10^{-19}J
ダルトン	Da	1 Da=1.660 538 86(28)×10^{-27}kg
統一原子質量単位	u	1 u=1 Da
天文単位	ua	1 ua=1.495 978 706 91(6)×10^{11}m

表８．SIに属さないが、SIと併用されるその他の単位

名称	記号	SI 単位で表される数値
バール	bar	1 bar=0.1MPa=100 kPa=10^5Pa
水銀柱ミリメートル	mmHg	1 mmHg≈133.322Pa
オングストローム	Å	1 Å=0.1nm=100pm=10^{-10}m
海里	M	1 M=1852m
バーン	b	1 b=100fm^2=(10^{-12}cm)^2=$10^{-28}m^2$
ノット	kn	1 kn=(1852/3600)m/s
ネーパ	Np	SI単位との数値的な関係は、対数量の定義に依存。
ベル	B	
デシベル	dB	

表９．固有の名称をもつCGS組立単位

名称	記号	SI 単位で表される数値
エルグ	erg	1 erg=10^{-7} J
ダイン	dyn	1 dyn=10^{-5}N
ポアズ	P	1 P=1 dyn s cm^{-2}=0.1Pa s
ストークス	St	1 St =1cm^2 s^{-1}=$10^{-4}m^2$ s^{-1}
スチルブ	sb	1 sb =1cd cm^{-2}=10^4cd m^{-2}
フォト	ph	1 ph=1cd sr cm^{-2} =10^4lx
ガル	Gal	1 Gal =1cm s^{-2}=$10^{-2}ms^{-2}$
マクスウエル	Mx	1 Mx = 1G cm^2=10^{-8}Wb
ガウス	G	1 G =1Mx cm^{-2} =10^{-4}T
エルステッド(a)	Oe	1 Oe ≙ (10^3/4π)A m^{-1}

(a) ３元系のCGS単位系とSIでは直接比較できないため、等号「 ≙ 」は対応関係を示すものである。

表10．SIに属さないその他の単位の例

名称	記号	SI 単位で表される数値
キュリー	Ci	1 Ci=3.7×10^{10}Bq
レントゲン	R	1 R = 2.58×10^{-4}C/kg
ラド	rad	1 rad=1cGy=10^{-2}Gy
レム	rem	1 rem=1 cSv=10^{-2}Sv
ガンマ	γ	1 γ=1 nT=10^{-9}T
フェルミ		1 フェルミ=1 fm=10^{-15}m
メートル系カラット		1 メートル系カラット= 0.2 g = 2×10^{-4}kg
トル	Torr	1 Torr = (101 325/760) Pa
標準大気圧	atm	1 atm = 101 325 Pa
カロリー	cal	1 cal=4.1858J（「15℃」カロリー），4.1868J（「IT」カロリー），4.184J（「熱化学」カロリー）
ミクロン	μ	1 μ =1μm=10^{-6}m

（第8版，2006年）